Laser-cluster interaction in an external magnetic field: Emergence of a nearly monoenergetic weakly relativistic electron beam

Kalyani Swain [1,2] S. S. Mahalik,[1,*] and M. Kundu [1,2]
[1] *Institute for Plasma Research, Bhat, Gandhinagar 382428, India*
[2] *Homi Bhabha National Institute, Training School Complex, Anushaktinagar, Mumbai 400094, India*

(Received 3 March 2023; revised 6 June 2023; accepted 11 October 2023; published 2 November 2023)

Recent studies [e.g., Sci. Rep. **12**, 11256 (2022)] on laser interaction (for a wavelength of 800 nm and intensity greater than 10^{16} W/cm^2) with a deuterium nanocluster in an ambient magnetic field B_0 demonstrate that collisionless absorption of laser light occurs in two stages via anharmonic resonance and electron-cyclotron resonance (ECR) or relativistic ECR (RECR) processes. The auxiliary magnetic field B_0 enhances the coupling of the laser field to cluster electrons via improved frequency matching for ECR or RECR as well as phase matching for the prolonged duration of the 5-fs (FWHM) broadband pulse. As a result, the average absorbed energy per electron $\overline{\mathscr{E}}$ significantly jumps up approximately 36–70 times its ponderomotive energy U_p. In this paper we report the energy dispersion of these energetic electrons and their angular distribution in position and momentum space by performing hybrid particle-in-cell simulations. By simulating bigger clusters (radius $R_0 \approx$ 3–4 nm) at high intensities of approximately 10^{16}–10^{18} W/cm^2, we find $\overline{\mathscr{E}} \approx 36U_\mathrm{p}$–$70U_\mathrm{p}$, which is similar to a small cluster ($R_0 \approx 2$ nm), but total energy absorption increases almost linearly with increasing cluster size due to the greater number of available energy carriers. In all cases near ECR or RECR, electrons form a narrow conelike weakly relativistic gyrating beam (about B_0) within an angular spread $\Delta\theta < 5^\circ$, propagating far beyond $200R_0$ along B_0. This study may be relevant because an intense, weakly relativistic electron beam has wide applications, including the fast ignition technique for inertial confinement fusion, ultrashort-x-ray sources, and medical applications.

DOI: 10.1103/PhysRevA.108.053104

I. INTRODUCTION

The interaction of an intense laser field with a cluster of atoms or molecules (called nanoclusters) constitutes a promising research area in strong-field wave-matter interactions. Atomic clusters with solidlike density may absorb 80–90 % of laser light [1]. Importantly, laser-cluster interaction (LCI) produces energetic ions [1–4], neutrals [5], electrons [2,6–9], and x rays [10–14]. Thus, it paves the way to future-generation particle accelerators and photon accelerators. Basic processes in LCI, i.e., (i) inner ionization, the birth of electrons leading to the formation of nanoplasma; (ii) outer ionization, removal of electrons from the whole cluster; and (iii) Coulomb explosion, acceleration of background ions, are described elsewhere [15–18] and not repeated here for the sake of conciseness.

For laser intensities $I_0 > 10^{16}$ W/cm^2 and wavelength $\lambda > 600$ nm, laser absorption in a cluster is mostly collisionless [19–22], wherein linear resonance and anharmonic resonance (AHR) may play an active role. Linear resonance happens [23–26] for a long laser pulse (typically greater than 50 fs) on the Coulomb explosion of an initially overdense ($\rho_\mathrm{i} > \rho_\mathrm{c}$) cluster when the ionic charge density $\rho_\mathrm{i}(t)$ gradually drops to the critical density $\rho_\mathrm{c} = \omega^2/4\pi$ and the Mie plasma frequency $\omega_\mathrm{M}(t) = \sqrt{4\pi\rho_\mathrm{i}/3}$ dynamically meets the laser frequency $\omega = 2\pi c/\lambda$. Atomic units (a.u.) $|e| = m_0 = \hbar = 4\pi\epsilon_0 = 1$ are used throughout unless explicitly noted otherwise. However, for short-pulse duration $\omega_\mathrm{M}(t) > \omega$ holds (the cluster is overdense) and AHR becomes important. During AHR, the oscillation frequency of an electron in the self-consistent anharmonic cluster potential meets ω. Anharmonic resonance has been noted in many works [27–33] using the rigid-sphere model (RSM), particle-in-cell (PIC) and molecular-dynamics (MD) simulations.

Though numerous experiments, analytical models, and numerical simulations have shown energetic electrons in the collisionless regime, our survey [34] reveals that the maximum average energy of a liberated electron mostly remains close to $3.17U_\mathrm{p}$ or below ($U_\mathrm{p} = I_0/4\omega^2$ is the ponderomotive energy of an electron), even if the laser has an adequate supply of energy. Note that this energy, near $3.17U_\mathrm{p}$, is similar to the maximum energy of a photoelectron upon its return to the parent ion in a monochromatic linearly polarized laser field in the laser-atom [35–38] interaction. In the case of a laser-deuterium cluster interaction [34], with a 5-fs broadband laser pulse (central $\lambda = 800$ nm and $I_0 \approx 10^{16}$–10^{18} W/cm^2) and an ambient magnetic field B_0 in crossed orientation to the laser electric field E_l, we have shown by the RSM and three-dimensional PIC simulation that enhanced laser absorption occurs in two stages: via AHR (first stage) and electron-cyclotron resonance (ECR) or relativistic ECR (RECR) processes (second stage). During the ECR or RECR, the electron-cyclotron frequency $\Omega_\mathrm{c} = |e|B_0/m_0\gamma = \Omega_{\mathrm{c}0}/\gamma$ meets ω, where $\Omega_{\mathrm{c}0} = |e|B_0/m_0$. For $\gamma = 1$, conventional ECR happens. The auxiliary B_0 enhances the coupling

*Present address: Bellatrix Aerospace Pvt. Ltd., Bangalore 560020, India.

2469-9926/2023/108(5)/053104(12)

of the laser to cluster electrons via improved frequency matching as well as phase matching, and the average absorbed energy per electron jumps to $\overline{\mathscr{E}} \approx 36U_p$–$70U_p$ (more than 12- to 36-fold [34]), which is significant.

One may argue that the required ambient $B_0 \approx 10$–20 kT is too high to achieve ECR or RECR in a laboratory with an 800-nm laser. However, with a CO_2 laser ($\lambda \approx 10.6$ μm), the strength of B_0 for the ECR or RECR is scaled down to $B_0 \approx 1$–2 kT, which seems feasible. The recent demonstration of pulsed magnetic fields [39–45] up to megatesla order has rekindled interest in the laser-plasma [46–48] community and may serve the purpose. In this context, we mention that self-generated (quasistatic) magnetic fields above 10 kT have also been noted in high-density laser-plasma experiments [49,50] and astrophysical conditions [51]. For example, self-generated magnetic fields in the range of 8–46 kT have been measured [49,50] with $I_0 \approx 10^{17}$–10^{20} W/cm^2, and for lower $I_0 \approx 10^{17}$–10^{19} W/cm^2, magnetic-field strengths B_0 lie in the range of 8–20 kT, which is of main interest here for the ECR or RECR absorption by electrons. Note that $B_0 \approx 40$ kT generated [50] at $I_0 \approx 10^{20}$ W/cm^2 is far from such resonances. Also, other experiments [39,52] have shown peak values of $B_0 \approx 15$–20 kT with $I_0 \approx (1$–$3) \times 10^{18}$ W/cm^2. Therefore, we choose closely consistent values of $I_0 \approx (7 \times 10^{16})$–$(2 \times 10^{18})$ W/cm^2 with $B_0 \approx 8$–26 kT, required for laser absorption by ECR or RECR for an 800-nm laser. There are also magnetic flux compression (MFC) schemes [42,53–55], currently being used in inertial confinement fusion to generate huge magnetic fields, which may be taken as ambient magnetic fields. We envisage that, after the generation of the ambient magnetic fields in step 1 either through laser-solid interactions [39,49,50,52] or using different coil assemblies [42,53–55] including MFC, a neutral cluster beam can be passed through it in step 2. Subsequently, it can be shot by a suitable laser pulse in step 3 with a time delay. These (pump-probe-like) ideas may require proper synchronization of the firing of lasers and time delay of injection of a cluster beam with extreme precision control in the desired interaction volume. Though we have chosen deuterium clusters, possibly nanoparticles may also be injected where the physics of ECR or RECR remains the same as in our studies. Since the probe laser beam (step 3) is independent of the process by which the ambient magnetic field is generated, one may independently choose its parameters (both wavelength and intensity) in the different regimes of interactions, including the ECR or RECR absorption as well. In the astrophysical scenario, magnetic fields around neutron stars and pulsars [51] typically vary around 10^1–10^5 kT. Understanding the origin of energetic electrons in these strong electromagnetic field conditions is also of fundamental interest. From the application point of view, energetic electrons produced by LCI via ECR or RECR in an ambient magnetic field can be helpful for table-top radiation sources (such as x rays), particle accelerators useful for medical applications, and inertial confinement fusion.

In the previous work [34], though it was shown that the average energy of laser-driven cluster electrons increases significantly ($\overline{\mathscr{E}} \approx 36U_p$–$70U_p$) with an ambient B_0 near ECR or RECR, it is not yet known how those electrons propagate together as a beam. The generation of a relativistic electron beam is also of current interest [56–58]. Therefore, understanding the energy distribution of ejected cluster electrons and their divergence (directional) properties is important from the point of view of applications as well as in the astrophysical scenario mentioned above. In this paper we report the energy dispersion of these energetic electrons and their angular distribution in position and momentum space by performing hybrid PIC simulations. The effect of ambient magnetic-field-driven ECR or RECR on different cluster sizes is also not known so far. This may be particularly important for higher electron flux as a narrow beam. By simulating bigger clusters of radius $R_0 \approx 3$–4 nm at intensities $I_0 \approx 10^{16}$–10^{18} W/cm^2, here we find that the average absorbed energy per electron jumps to approximately $36U_p$–$70U_p$, which is similar to a small cluster ($R_0 \approx 2$ nm). However, the total energy absorption increases almost linearly with increasing cluster size due to the higher number of available energy carriers. In all cases near ECR or RECR, electrons form a weakly relativistic gyrating narrow beam (about B_0) within an angular spread $\Delta\theta < 5^\circ$, propagating far beyond $200R_0$ along B_0. These PIC results are further supported by the RSM.

In Sec. II laser pulse and cluster parameters are given. In Sec. III we discuss the details of the PIC simulation code and its hybrid capability for treating particle interactions outside the simulation box. Section IV focuses on the energy distribution of electrons and their angular distribution in position space (as well as in momentum space) corresponding to the laser energy absorption by electrons for different ambient B_0. In Sec. V laser energy absorption for bigger clusters and associated angular distributions of ejected electrons are compared at high intensities. Section VI provides a summary. A brief description of the RSM is given in the Appendix.

II. LASER PULSE AND CLUSTER PARAMETERS

A laser pulse [34,59,60] is assumed to be propagating in the z direction and polarized in the x direction with vector potential $\boldsymbol{A}_l(t') = \hat{\boldsymbol{x}}(E_0/\omega)\sin^2(\omega t'/2n)\cos(\omega t')$ for $0 \leqslant t' \leqslant nT$, where $t' = t - z/c$, n is the number of laser periods T, $\tau = nT$ is the pulse duration, and $E_0 = \sqrt{I_0}$ is the field strength. Laser electric and magnetic fields $\boldsymbol{E}_l$ and $\boldsymbol{B}_l$, respectively, are obtained as

$$\boldsymbol{E}_l(t') = -\frac{\partial \boldsymbol{A}_l}{\partial t}, \quad \boldsymbol{B}_l(t') = \hat{\boldsymbol{z}} \times \boldsymbol{E}_l(t')/c. \tag{1}$$

The broadband nature of the pulse is understood from its discrete frequencies $\omega_1 = \omega$, $\omega_2 = (1 + 1/n)\omega$, and $\omega_3 = (1 - 1/n)\omega$. The sidebands are significant for short pulses.

Deuterium clusters of different sizes and numbers of atoms $N = 2176, 7208, 17256$ are chosen. According to the Wigner-Seitz radius $r_w \approx 0.17$ nm, the respective cluster radii are $R_0 = r_w N^{1/3} \approx 2.2, 3.3, 4.4$ nm. For $R_0 \ll \lambda$, the dipole approximation $z/\lambda \ll 1$ may be assumed. A single cluster is illuminated by the above laser pulse of $\lambda = 800$ nm for $n = 5$ and $\tau = nT \approx 13.5$ fs ($\tau_{\mathrm{FWHM}} \sim 5$ fs). A cluster is $\rho_i/\rho_c \approx 27.1$ times overdense with $(\omega_M/\omega)^2 \approx 9.1$, where $\rho_c \approx 1.75 \times 10^{27}$ m^{-3} is the critical density at $\lambda = 800$ nm.

III. PARTICLE-IN-CELL SIMULATION

We use three-dimensional (3D) PIC simulation code [29,30,34,59,61–64] for the LCI with and without ambient magnetic field $\boldsymbol{B}_{\mathrm{ext}}$. Different deuterium clusters with

$N = 2176$, 7208, and 17 256 are placed in a cubical computational box. The center of a cluster coincides with the center of the computational box. At first, ionization of neutral deuterium atoms from D to D^+ happens via over-the-barrier ionization (OBI) [65] by the laser field $\boldsymbol{E}_l(t)$ when a critical strength $E_c = |\boldsymbol{E}_l(t)| = I_p^2(Z)/4Z$ is reached (valid for $I_0 > 10^{15}$ W/cm^2). Here $I_p(Z)$ is the ionization potential for the charge state $Z = 1$. The position and velocity of a newly born electron (after the OBI) are assumed to be the same as the parent atom or ion, conserving momentum and energy. Subsequent movement of electrons and ions by the driving fields creates or modifies the space-charge field $\boldsymbol{E}_{sc}(\boldsymbol{r}, t) = -\nabla\phi(\boldsymbol{r}, t)$ and corresponding potential $\phi(\boldsymbol{r}, t)$, which are time dependent and start from zero.

The charge-to-mass ratio of a PIC electron or ion is identical to that of a real electron or ion. For the $j|k$th PIC electron or ion, the equations of motion are given by (j for electron and k for ion)

$$\frac{d\boldsymbol{p}_{j|k}}{dt} = q_{j|k}\{[\boldsymbol{E}_l(t) + \boldsymbol{E}_{sc}(\boldsymbol{r}_{j|k}, t)] + \boldsymbol{v}_{j|k} \times (\boldsymbol{B}_l + \boldsymbol{B}_{\text{ext}})\}, \tag{2}$$

$$\frac{d\boldsymbol{r}_{j|k}}{dt} = \boldsymbol{v}_{j|k} = \frac{\boldsymbol{p}_{j|k}}{\gamma_{j|k} m_{j|k}}, \tag{3}$$

where $\boldsymbol{p}_{j|k} = m_{j|k}\boldsymbol{v}_{j|k}\gamma_{j|k}, \boldsymbol{v}_{j|k}, \boldsymbol{r}_{j|k}, m_{j|k}, q_{j|k}, \gamma_{j|k}$ are momentum, velocity, position, mass, and charge of a PIC electron or ion and $\gamma_{j|k} = \sqrt{1 + p_{j|k}^2/m_{j|k}^2 c^2}$, respectively. In the present case, $m_j = m_0 = 1$, $m_k = M_0 = 2 \times 1386$, $q_j = -1$, and $q_k = 1$ in a.u. We solve Poisson's equation $\nabla^2\phi_G = -\rho_G$ on the numerical grids using time-dependent monopole boundary conditions to obtain the potential ϕ_G. The subscript G denotes grid values of potential ϕ and charge density ρ. Then we calculate the potential $\phi(\boldsymbol{r}_{j|k}, t)$ by interpolating ϕ_G to the particle position, and from this interpolated $\phi(\boldsymbol{r}_{j|k})$ the corresponding field $\boldsymbol{E}_{sc}(\boldsymbol{r}_{j|k}) = -\nabla\phi(\boldsymbol{r}_{j|k})$ is obtained locally at $\boldsymbol{r}_{j|k}$ by analytical differentiation [64]. Equations (2) and (3) are solved by the velocity Verlet method (VVM) using laser fields (1). Note that, even for a larger Δt, especially for relativistically intense driving fields, the VVM provides better energy conservation and hence less numerical heating. As the field strength is very high, electron-ion collisions are less effective in the present work. The total absorbed energy $\mathscr{E}(t) = \sum_l q_l\phi_l + p_l^2/2m_l$ is obtained by summing over the kinetic energy KE $= \sum_l p_l^2/2m_l$ and potential energy PE $= \sum_l q_l\phi_l$ of all electrons and ions. The contribution of ion kinetic energy is negligibly small for the five-cycle pulse (used here) and electrons account for the majority of the total energy. The final absorbed energy $\mathscr{E}_A = \mathscr{E}(\tau)$ in the end of the laser pulse at $\tau = nT$ is also noted. The temporal resolution, grid size, number of PIC particles per cell, and other numerical parameters in the PIC simulation are carefully chosen for minimal artificial numerical heating. In this work we take approximately 15 particles per cell with uniform cell size (spatial grid) $\Delta x = \Delta y = \Delta z = 16$ a.u., time step $\Delta t = 0.1$ a.u., and 64^3 (128^3 for bigger cluster) grid points.

Hybrid PIC simulations

In the PIC simulation, the treatment of particles crossing or leaving the boundaries of the simulation box needs special care. Often, reflecting or periodic boundary conditions are used, which preserve particles inside the simulation box, and the Poisson equation with appropriate boundary conditions takes care of the space-charge field $\boldsymbol{E}_{sc}(\boldsymbol{r}_{j|k})$ on an inside particle. For a finite-size target (e.g., cluster), in early works we used open boundary conditions for particles. This means that particles that leave the simulation box are free from space-charge fields $\boldsymbol{E}_{sc}(\boldsymbol{r}_{j|k})$. This assumption tests valid for the short laser pulse by keeping a simulation box size $L \approx 16R_0$–$20R_0$ (typically) beyond which $\boldsymbol{E}_{sc} \approx 0$. It also allows particles (particularly electrons) to go back inside the box or propagate similarly to direct laser acceleration (DLA) outside the box obeying (2) and (3). For a dense electron cloud outside the simulation box (in a strong ambient B_0), electron-electron interaction (repulsion) may be important for the divergence or collimation of the electron beam. Therefore, we adapt a hybrid procedure to determine $\boldsymbol{E}_{sc}$ on an electron. As long as the electron is inside the box, $\boldsymbol{E}_{sc}$ is solely determined by the standard PIC approach. When it is outside the box, $\boldsymbol{E}_{sc}$ is determined by the field due to the total charge (including ions and electrons) inside the simulation box (monopole field) plus the fields due to all other electrons outside the simulation box as in MD simulations [33].

IV. LASER ABSORPTION IN CLUSTERS IN AMBIENT MAGNETIC FIELDS

A deuterium cluster of $N = 2176$ and $R_0 = 2.2$ nm is irradiated by an $n = 5$ cycle laser pulse of $I_0 = 7.13 \times 10^{16}$ W/cm^2 in the presence of ambient magnetic fields $\boldsymbol{B}_{\text{ext}} = B_0\hat{z}$ along the laser propagation direction z for different values of B_0. Figure 1 shows total absorbed energy $\overline{\mathscr{E}_A} = \mathscr{E}_A/NU_p$ per electron [TE, green (light gray)] in units of U_p vs normalized electron-cyclotron frequency Ω_{c0}/ω obtained with PIC simulation (solid lines) and the RSM (dashed lines). Let us explain the PIC results first. Note that $\Omega_{c0} = B_0$ in a.u. At lower B_0 (or without B_0), absorption is very poor, $\overline{\mathscr{E}_A} \approx 0.5$ at point A. It gradually increases to $\overline{\mathscr{E}_A} \approx 36$ at B for ECR (vertical dashed line, where $\Omega_{c0}/\omega = 1$) and reaches a peak $\overline{\mathscr{E}_A} \approx 68$ at C for $\Omega_{c0}/\omega \approx 1.25$. The ratio of absorbed energies at B and C to that at A are $\overline{\mathscr{E}_A}(B)/\overline{\mathscr{E}_A}(A) \approx 72$ and $\overline{\mathscr{E}_A}(C)/\overline{\mathscr{E}_A}(A) \approx 136$, respectively. Thus, strong ambient magnetic fields may enhance laser absorption approximately 70- to 136-fold for a cluster. Compared to the laser-atom interaction [35–38], where the maximum photoelectron energy of an electron returned to the parent ion is approximately $3.17U_p$, these $\overline{\mathscr{E}_A}$ values are approximately 12- to 23-fold in the case of LCI. Though the magnetic field does not work, it reorients phase-space coordinates $(\boldsymbol{r}_{j|k}, \boldsymbol{v}_{j|k})$ of a charged particle (particularly for an electron) and hence may improve the rate of laser absorption, obeying the relation

$$\frac{d(\gamma_{j|k} m_{j|k} c^2)}{dt} = q_{j|k}\boldsymbol{v}_{j|k} \cdot [\boldsymbol{E}_l(t) + \boldsymbol{E}_{sc}(\boldsymbol{r}_{j|k}, t)], \tag{4}$$

through improved phase matching [34] between $\boldsymbol{v}_{j|k}$ and the total field $\boldsymbol{E} = \boldsymbol{E}_l(t) + \boldsymbol{E}_{sc}(\boldsymbol{r}_{j|k}, t)$. Equation (4) is fundamental for the transfer of energy to a charged particle from the interacting fields. Self-consistent $\boldsymbol{E}_{sc}(\boldsymbol{r}_{j|k}, t)$ is nonlinear in general and falls quickly as $1/r^2$ after a few times of the cluster radius R_0. Anharmonic resonance absorption [34] of

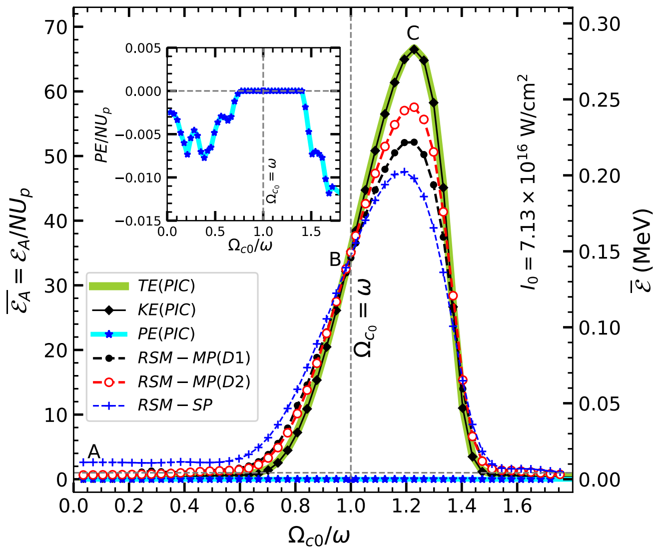

FIG. 1. PIC and RSM results. The average total energy $\overline{\mathscr{E}}_A$, kinetic energy, and potential energy per cluster electron are plotted vs normalized electron-cyclotron frequency Ω_{c0}/ω for a range of ambient field $|\hat{z}B_{\rm ext}| \approx 0$–$2\omega$ with an $n = 5$ cycle pulse of $I_0 \approx 7.13 \times 10^{16}$ W/cm^2 irradiating a deuterium cluster of $N = 2176$ and $R_0 = 2.2$ nm. Energy is normalized by the corresponding $U_{\rm p}$. At low I_0, the absorption peak occurs almost at the ECR condition $\Omega_{c0} = \omega$ (vertical dashed line; see Ref. [34]), whereas at high $I_0 \approx 7.13 \times 10^{16}$ W/cm^2, the absorption peak is right shifted from the ECR condition $\Omega_{c0} = \omega$ due to relativistic modification of $\Omega_c = \Omega_{c0}/\gamma$ for $\gamma > 1$. An absorption peak near $65U_{\rm p}$ gives an average energy per electron 0.27 MeV (right axis). The inset shows a negligibly small average PE per electron; thus, the TE is mainly due to KE. The RSM results (dashed lines) with single-electron dynamics (RSM-SP, -+-) and multielectron dynamics (RSM-MP) with two different initial electron distributions (D1, uniform distribution, -•-) and (D2, PIC-like distribution, -○-) are also shown for comparison with the PIC results.

the laser by an electron happens within this nonlinear field and may be modified [34] by an ambient $\boldsymbol{B}_{\rm ext}$. After leaving the cluster via AHR (called the first stage [34]) with some transverse momentum, electrons are mainly controlled by the remaining $\boldsymbol{E}_l$, $\boldsymbol{B}_l$, $\boldsymbol{B}_{\rm ext}$, and weak $\boldsymbol{E}_{sc}$ outside, and there ECR or RECR may happen (called the second stage [34]), resulting in enhanced laser absorption as in Fig. 1. The results of simultaneous phase-matching and frequency-matching conditions for these absorption processes have already been given in Ref. [34] for similar parameters and not repeated here for the sake of conciseness.

We also partition the total absorbed energy [TE, green (light gray)] into electron kinetic [KE, thin black line with diamonds] and potential energy [PE, light blue line (gray) with stars] in Fig. 1. It shows that the main contribution comes from the electron's kinetic energy. Acceleration of these electrons by ECR or RECR (in the second stage) resembles magnetic-field-assisted DLA of electrons. However, in the present case, electrons originate from the overdense cluster, self-injected into the remaining laser field in the presence of ambient $\boldsymbol{B}_{\rm ext}$, and no external injection mechanism is required. It is important to mention that most of the models for DLA of electrons consider an underdense, preformed plasma channel [47,66–70] or single electron without considering particle interactions.

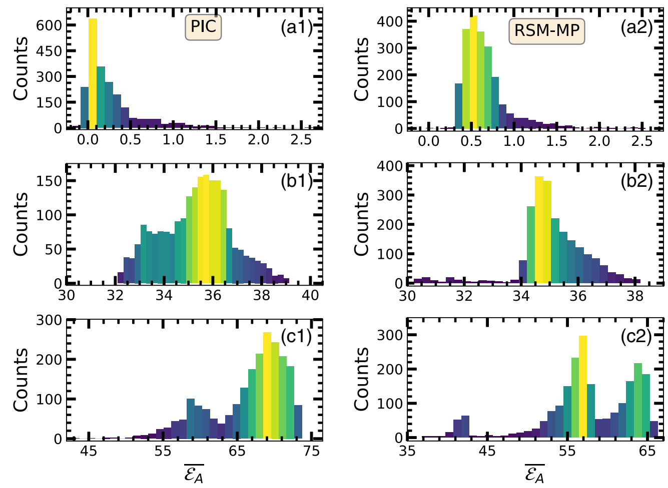

FIG. 2. Energy distribution of (a1)–(c1) PIC electrons and (a2)–(c2) RSM-MP electrons, using a PIC-like initial distribution, ejected from the deuterium cluster corresponding to the ambient magnetic fields $B_0 \approx 0.02, 0.057, 0.07$ a.u. (at A, B, and C in Fig. 1). The yellow (light gray) region highlights maximum electron counts and respective energies $\overline{\mathscr{E}}_A$. The other parameters are the same as in Fig. 1.

In Fig. 1 the PIC results for total absorbed energy are also compared for the RSM (dashed line) using single-electron (RSM-SP) and multielectron (RSM-MP) dynamics with two different initial electron distributions (D1, uniform distribution) and (D2, PIC-like distribution). Clearly, RSM-MP(D2) shows a better match with the full 3D PIC result (see also the Appendix).

A. Energy distribution of electrons

Figures 2(a)–2(c) show the energy distribution of PIC electrons [Figs. 2(a1)–2(c1)] and RSM-MP electrons [Figs. 2(a2)–2(c2)] corresponding to the chosen data points A, B, and C in Fig. 1 for $B_0 \approx 0.35\omega, \omega, 1.25\omega$, respectively. For a given $I_0 = 7.13 \times 10^{16}$ W/cm^2, the energy distribution of electrons is gradually modified as B_0 increases. With a low value of B_0 (or without it, for A), more electrons [yellow (light gray) region] are near lower energy $\overline{\mathscr{E}}_A \approx 0.1, 0.5$ for the PIC simulation and RSM, respectively; however, the energy tail with a few electrons extends up to $\overline{\mathscr{E}}_A \approx 2.6$. This is the typical energy distribution of electrons one mostly finds in the case of LCI with a very low B_0 (or without B_0). On the other hand, for higher B_0 values corresponding to B and C, more electrons are pushed around $\overline{\mathscr{E}}_A \approx 36$ and $\overline{\mathscr{E}}_A \approx 68$ with PIC simulation and $\overline{\mathscr{E}}_A \approx 35$ and $\overline{\mathscr{E}}_A \approx 58$ with the RSM-MP, respectively. Thus, there is a reversal in the nature of energy distribution while passing from A to C. The integrated average energy values of $\overline{\mathscr{E}}_A$ from these distributions are found to satisfy the respective $\overline{\mathscr{E}}_A$ at A, B, and C in Fig. 1. These groups of electrons will now be thoroughly analyzed to understand their divergence (and propagation) as a beam. One can find that the energy distribution of electrons with the RSM-MP (for PIC-like initial conditions) exhibits a similar nature of energy distribution as in the PIC simulation (though not exact). For other initial distributions of electrons (uniform or random), the RSM-MP yields even a poor match (not shown here) with the PIC data. With the RSM-SP, one finds only a single point [near the yellow (light gray) region] on the energy distribution, but it does not show the details of the distribution (Fig. 2). Therefore, the RSM-MP with PIC-like initial conditions is used in the rest of the paper, unless explicitly noted otherwise.

B. Angular distribution of electrons

Angular deflection of an electron (θ_r) in the position space is defined as the angle between the laser light propagation in the z direction (which is also the direction of $\boldsymbol{B}_{\text{ext}} = B_0\hat{z}$) and its position vector $\boldsymbol{r}$. This elevation angle can be obtained from

$$z = r\cos\theta_r, \quad r_\perp = r\sin\theta_r, \tag{5}$$

where $r_\perp = \sqrt{x^2 + y^2}$.

We calculate (r, θ_r) for all PIC and RSM-MP electrons. Figure 3 shows histograms of electrons versus θ_r for the PIC simulation and RSM-MP (left column) and respective polar plots (right column) with their normalized position r/R_0 vs θ_r corresponding to those energy spectra in Figs. 2(a)–2(c). Polar coordinates (r, θ_r) are color coded with their energy normalized by U_p. For lower $B_0 = 0.02$ a.u., electrons are spread over a wide angular range $\theta_r \approx 0$–175° and [Figs. 3(a1) and 3(r-a1)] for the PIC simulation and RSM-MP, respectively. Note that the RSM results are distinguished by an additional label "r" [i.e., (r-a1)–(r-c1) and (r-a2)–(r-c2)]. The distribution in the (r, θ_r) plane explains that the angular spread contains only low-energy electrons (for the PIC simulation and RSM-MP) due to the weak coupling of the laser light to the cluster electrons at lower B_0 values [Figs. 3(a2) and 3(r-a2)]. As the magnetic field increases to $B_0 = 0.057$ a. u. [Figs. 3(b1), 3(b2), 3(r-b1), and 3(r-b2)] and $B_0 = 0.07$ a.u. [Figs. 3(c1), 3(c2), 3(r-c1), and 3(r-c2)], these electrons align themselves more towards the magnetic-field direction z. They propagate at $r \approx 375R_0, 500R_0$ [Figs. 3(b2) and 3(c2)] and $r \approx 350R_0, 450R_0$ [Figs. 3(r-b2) and 3(r-c2)] within an angular spread of $\Delta\theta_r < 3^\circ$ centered around narrow cone angles $\theta_r \approx 7^\circ$–8.5° for PIC simulation and RSM-MP, respectively. This demonstrates that the ambient magnetic field near ECR or RECR probes the ejected electrons to form a narrow conical beam gyrating about the z axis as well as propagating in the z direction in the position space like a spiral. For $B_0 = 0.057$ and 0.07 a.u., the energy of most of the electrons in these beams in Figs. 3(b2), 3(c2), 3(r-b2), and 3(r-c2) shows a maximum value of absorption that satisfies the energy distribution peaks in Figs. 2(b) and 2(c) for PIC and RSM-MP results, respectively. Differences between the PIC and RSM-MP results are significant [Figs. 3(a1), 3(a2), 3(r-a1), and 3(r-a2)] for lower B_0 values. For high B_0 values the PIC results [Figs. 3(b1), 3(b2), 3(c1), and 3(c2)] are well predicted by the respective RSM-MP results [Figs. 3(r-b1), 3(r-b2), 3(r-c1), and 3(r-c2)].

The conical beam of electrons can also be explained by the angular deflection θ_p of the momentum $\boldsymbol{p}$ of an electron with respect to z. With transverse momentum (p_x, p_y) and

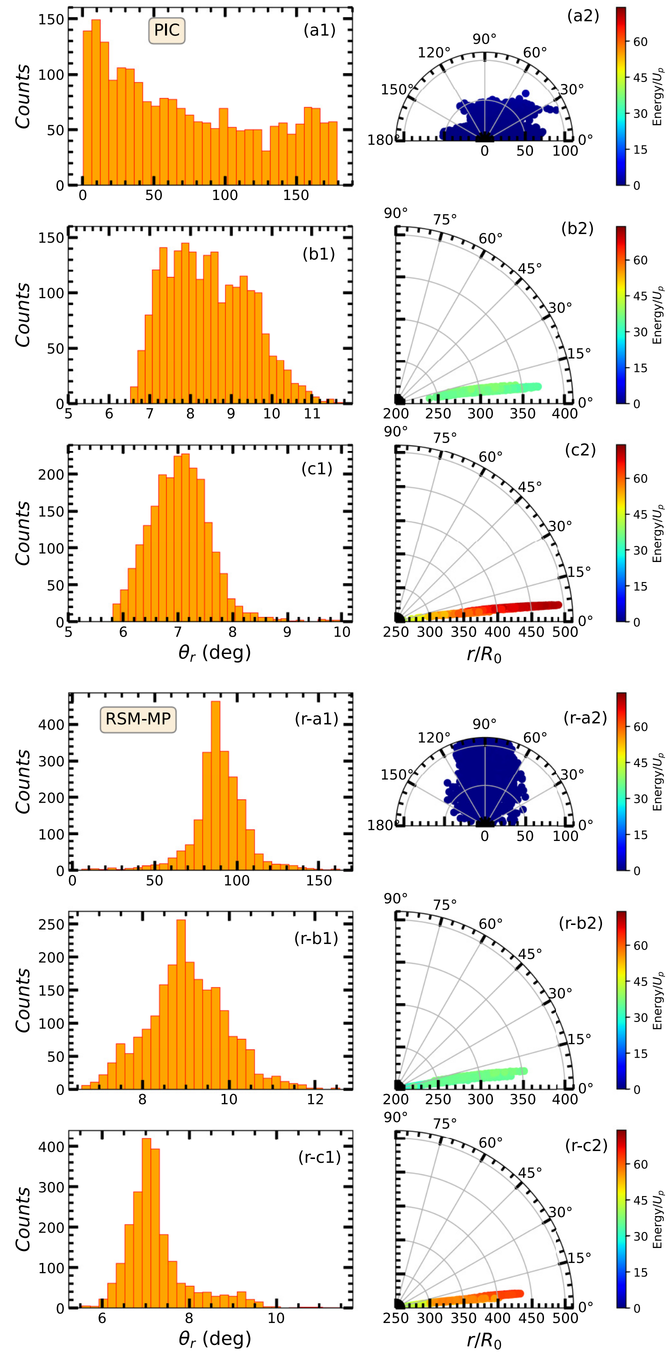

FIG. 3. Histograms showing the distributions of angular deflection θ_r of PIC and RSM-MP electrons (left column) and respective polar plots (right column) with their normalized position r/R_0 vs θ_r corresponding to those energy spectra in Figs. 2(a)–2(c) for $B_0 =$ 0.02, 0.057, 0.07 a.u., respectively. Polar coordinates (r, θ_r) are color coded with their energy normalized by U_p. Ejected electrons propagate a long distance [(b2) and (c2)] $r = \sqrt{r_\perp^2 + z^2} \approx 375R_0, 500R_0$ for the PIC simulation, and [(r-b2) and (r-c2)] $r \approx 350R_0, 450R_0$ for the RSM-MP simulation as narrow gyrating beams with angular spreads $\Delta\theta_r < 3^\circ$ centered around $\theta_r \approx 7^\circ$–8.5° for the PIC and $\theta_r \approx 7^\circ$–9° for the RSM-MP simulation, respectively. The other parameters are the same as in Figs. 1 and 2. Note that the RSM results are distinguished by an additional label "r" [i.e., (r-a1)–(r-c1) and (r-a2)–(r-c2)].

longitudinal momentum (p_z), one obtains θ_p from

$$p_z = p\cos\theta_p, \quad p_\perp = p\sin\theta_p, \tag{6}$$

where $p_\perp = \sqrt{p_x^2 + p_y^2}$. Importantly, the angle θ_p is often more physically relevant than θ_r to determine the transport properties of electrons and the kind of magnetic configuration required to transport these electrons as a beam. However, position coordinates (r, θ_r) of electrons are also important to know how far these electrons have been transported as a beam and at what orientation. Figure 4 shows histograms of PIC and RSM-MP electrons (left column) and respective polar plots (right column) with their normalized momentum p/c vs θ_p corresponding to those spectra in Fig. 3. Coordinates (p, θ_p) are color coded with their energy normalized by U_p. For $B_0 = 0.02$ a.u., there is a wide angular spread centered around $\theta_p \approx 90^\circ$, for both the PIC simulation and RSM-MP, with low-energy electrons in Figs. 4(a1), 4(a2), 4(r-a1), and 4(r-a2). This wide cone angle with θ_p is expected in the case of a rotational motion of a low-energy electron near the xy plane where its spiral-like conical evolution along the $+z$ axis is still not significant. However, for higher magnetic fields $B_0 = 0.057$ a.u. in Figs. 4(b1), 4(b2), 4(r-b1), and 4(r-b2); and $B_0 = 0.07$ a.u. in Figs. 4(c1), 4(c2), 4(r-c1), and 4(r-c2), conical beams of high-energy electrons are formed in the momentum space with angular spread $\Delta\theta_p < 5^\circ$ similar to $\Delta\theta_r < 5^\circ$ in the position space. The cone angle θ_p now changes towards 63°–69°, meaning that all electrons gyrate around the surface of the cone with a little spread of $\Delta\theta_p < 5^\circ$ and spirally propagate in the z direction with increasing energy. The momentum of beam electrons reaches weakly relativistic values $p = \sqrt{p_\perp^2 + p_z^2} \approx 0.875c, 1.25c$ [Figs. 4(b2) and 4(c2)] for the PIC simulation and $p \approx 0.85c, 1.20c$ [Figs. 4(r-b2) and 4(r-c2)] for the RSM-MP even with a short five-cycle laser pulse of intensity $I_0 \approx 7.13 \times 10^{16}$ W/cm^2. We find that momentum distributions in (p, θ_p) are very well predicted by the RSM-MP (see the caption of Fig. 4), which corroborate the respective PIC spectra. Thus, the origin of a narrow conical beam of cluster electrons in the position space with a wide cone angle in the momentum space in the PIC simulation is justified by the RSM-MP in the presence of high ambient magnetic fields near the ECR or RECR.

V. EFFECTS OF CLUSTER SIZE VARIATION

In a realistic scenario, cluster size may vary. The effect of ECR or RECR with an ambient magnetic field on different cluster sizes is not known. In particular, it is important to know whether a bigger cluster absorbs more laser energy via ECR or RECR compared to a smaller cluster of $R_0 \approx 2.2$ nm in Sec. IV. Therefore, we simulate bigger deuterium clusters of $R_0 \approx 3.3, 4.4$ nm with numbers of atoms $N = 7208, 17\,256$, respectively. However, to accommodate bigger clusters as well as to obtain good accuracy, we now increase the number of computational grids to 128^3 and the simulation box size to 2048^3 a.u. in the PIC simulation, keeping other simulation parameters and configurations the same as the smaller cluster in Sec. IV. To corroborate the PIC results, we also simulate the same clusters with the RSM.

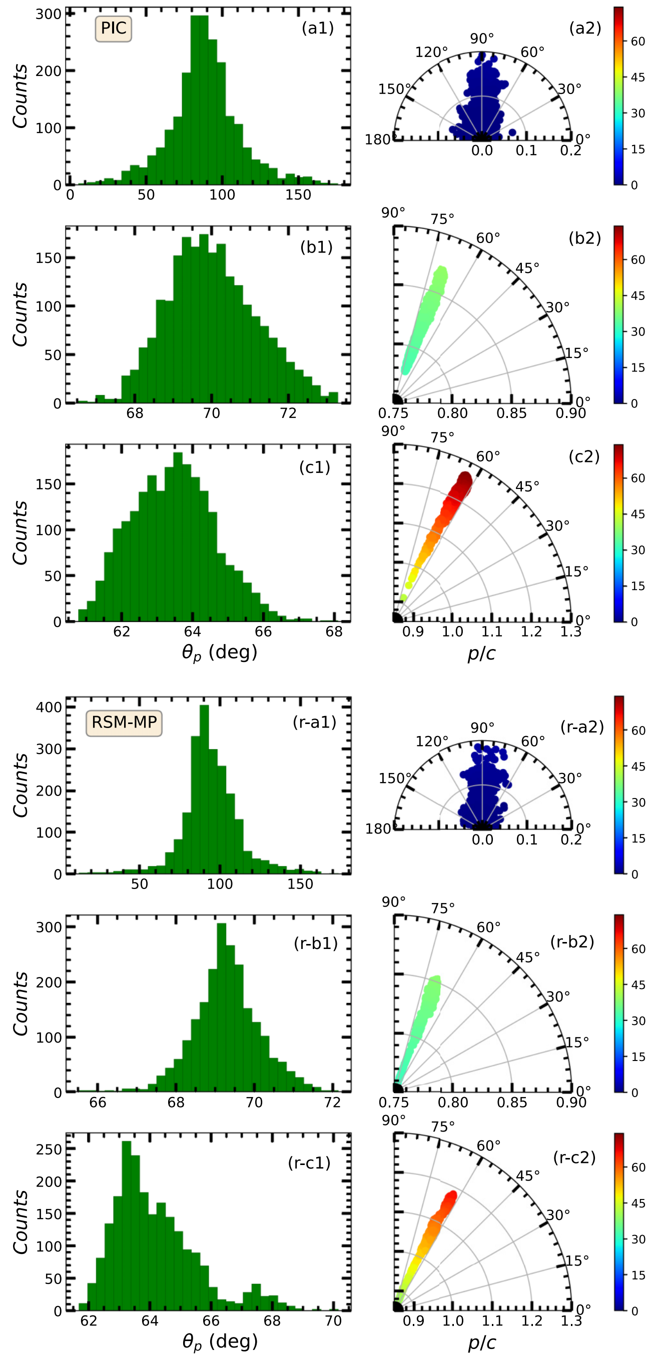

FIG. 4. Histograms showing the distributions of angular deflection θ_p of PIC and RSM-MP electrons (left column) in the momentum space and respective polar plots (right column) with their normalized momentum p/c vs θ_p corresponding to the energy spectra in Figs. 2(a)–2(c) for $B_0 = 0.02, 0.057, 0.07$ a.u., respectively. Coordinates (p, θ_p) are color coded with their energy normalized by U_p. The momentum of ejected electrons reaches [(b2) and (c2)] $p = \sqrt{p_\perp^2 + p_z^2} \approx 0.875c, 1.25c$ for the PIC and [(r-b2) and (r-c2)] $p \approx 0.85c, 1.2c$ for the RSM-MP simulation with angular spreads $\Delta\theta_p < 4^\circ$ centered around $\theta_p \approx 70^\circ$–$64^\circ$ for the PIC and $\theta_p \approx 69^\circ$–$64^\circ$ for the RSM-MP simulation, respectively. The other parameters are the same as in Figs. 1 and 2. Note that the RSM results are distinguished by an additional label "r" [i.e., (r-a1)–(r-c1) and (r-a2)–(r-c2)].

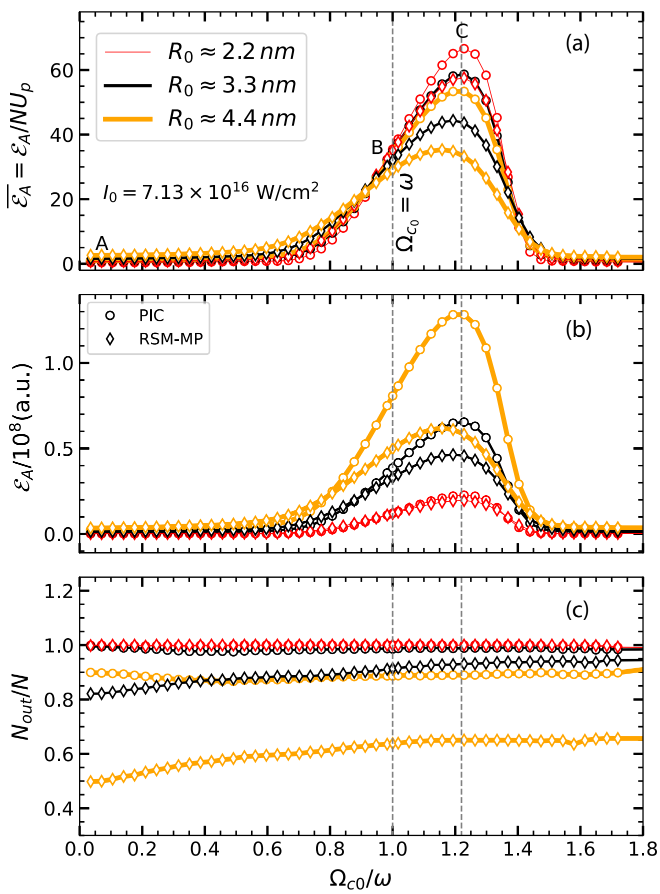

FIG. 5. PIC (○) and RSM (◇) results for different cluster sizes with $I_0 = 7.13 \times 10^{16}$ W/cm^2: (a) average total energy ($\overline{\mathscr{E}_A} = \mathscr{E}_A/NU_\mathrm{p}$) per cluster electron in units of U_p, (b) absorbed total energy $\mathscr{E}_A$ in the cluster scaled down by 10^8, and (c) fractional outer ionization of electrons (N_out/N) vs normalized electron-cyclotron frequency Ω_{c0}/ω for a range of ambient field $|\hat{z}B_\mathrm{ext}| \approx 0$–$2\omega$ for cluster sizes $R_0 \approx 2.2, 3.3, 4.4$ nm and the respective numbers of atoms $N = 2176, 7208, 17\,256$. An absorption peak near $65U_\mathrm{p}$ gives an average energy per electron 0.27 MeV. The other parameters are the same as in Fig. 1.

Figures 5(a)–5(c) show the comparison of absorption per electron $\overline{\mathscr{E}_A} = \mathscr{E}_A/NU_p$, total absorption $\mathscr{E}_A$, and outer ionized fraction N_out/N of electrons, respectively, vs Ω_{c0}/ω of three different cluster sizes for a range of $B_0 = 0$–2ω at the end of an $n = 5$ cycle pulse of intensity $I_0 = 7.13 \times 10^{16}$ W/cm^2 with the PIC simulation (circles) and RSM-MP (diamonds). Here N_out is the number of free electrons that have left the cluster boundary. Increasing cluster size does not significantly affect the absorption peak location [Figs. 5(a) and 5(b)] and the value of electron energy $\overline{\mathscr{E}_A}$ up to ECR [Fig. 5(a)]. The maximum absorption per electron [max($\overline{\mathscr{E}_A}$)] at the peak gradually drops to approximately 68, 59, 54 for the PIC simulation and max($\overline{\mathscr{E}_A}$) ≈ 60, 45, 35 for the RSM-MP as cluster size increases $R_0 = 2.2, 3.3, 4.4$ nm [Fig. 5(a)], which is partly due to fewer outer-ionized electrons (N_out) for the bigger cluster. The outer ionization of the $R_0 \approx 4.4$ nm cluster [Fig. 5(c)] at this $I_0 = 7.13 \times 10^{16}$ W/cm^2 is approximately 85–90 %, which means mainly 85–90 % of PIC and 50–65 % of RSM-MP electrons contribute to the total energy absorption. However, for the $R_0 \approx 2.2, 3.3$ nm clusters, outer ionizations are around 100% and 98%, respectively for the PIC simulation, indicating that nearly all electrons contribute to the energy absorption. In contrast, the RSM-MP predicts nearly 100% and 85%, leading to gradually increasing deviation of the RSM-MP from the PIC absorption curve as the cluster size increases. Additionally, the restoring force on electrons due to background ions gradually increases as the cluster size increases. This yields a higher per electron energy [Fig. 5(a)] at the peak with max($\overline{\mathscr{E}_A}$) ≈ 68 for a smaller $R_0 \approx 2.2$ nm cluster compared to max($\overline{\mathscr{E}_A}$) ≈ 48 for a bigger $R_0 \approx 4.4$ nm cluster in the case of the PIC simulation. Similarly, respective values are max($\overline{\mathscr{E}_A}$) ≈ 60, 35 for the RSM-MP. In contrast, the total energy absorption $\mathscr{E}_A$ by electrons [Fig. 5(b)] gradually increases with increasing cluster size at a given B_0, and for a bigger cluster it is significantly higher at the peak due to more energy carriers (N_out) after the outer ionization.

For many applications, a higher flux of energetic electrons as a narrow beam may be required, and bigger clusters may supply them. Therefore, in Fig. 6 we plot histograms for the angular distribution of PIC electrons and corresponding polar plots (in the insets) for $R_0 = 3.3, 4.4$ nm clusters as in Fig. 3 with a 2.2-nm cluster. These results correspond to $B_0 \approx 0.057$ a.u. [at B in Fig. 5(a)] and $B_0 \approx 0.07$ a.u. [at C in Fig. 5(a)] in the (r, θ_r) space [Figs. 6(a1), 6(b1), 6(a2), and 6(b2)] and (p, θ_p) space [Figs. 6(a1′), 6(b1′), 6(a2′), and 6(b2′)], respectively. Angular distributions of RSM-MP electrons are postponed here. Compared to the 2.2-nm cluster (Fig. 3), the angular spread $\Delta\theta_r$ is a little wider for larger clusters (Fig. 6), but there are now more energetic electrons within $\theta_r \approx 8°$–$12°$. In the case of the 3.3-nm cluster for $B_0 = 0.057, 0.07$ a.u. [Figs. 6(a1) and 6(b1)] the range of θ_r is almost the same; however, the electron beam with $B_0 = 0.07$ a.u. contains a higher number (approximately 3300) of energetic electrons around $\theta_r \approx 8°$. For the 4.4-nm cluster, due to its bigger size, the energetic electron population in the beam increases near 5000 and 6000 for $B_0 = 0.057, 0.07$ a.u. [Figs. 6(a2) and 6(b2)] around $\theta_r \approx 8°$. Similar findings apply for momentum distributions [Figs. 6(a1′), 6(b1′), 6(a2′), and 6(b2′)] also with wide-cone angles θ_p. It is clear that electrons propagate a distance $r \approx 350R_0, 280R_0$ [Figs. 6(b1) and 6(b2)] with respective $p \approx 1.25c, 1.25c$ [Figs. 6(b1′) and 6(b2′)] as conical-spiral beams with narrow angular spreads $\Delta\theta_r < 3°$ and $\Delta\theta_p < 4°$ centered around $\theta_r \approx 7°$–$8°$ and $\theta_p \approx 63°$–$67°$, respectively. The energy of an electron reaches around $1.25m_0c^2$ for $\gamma = p/c \approx 1.25$. We may conclude that the conical-spiral beams of electrons become more intense with a greater number of energetic electrons as cluster size increases, which may not be possible without ambient B_0.

Effects at high intensity

The results in the previous sections were obtained with $I_0 = 7.13 \times 10^{16}$ W/cm^2. In the case of the 4.4-nm cluster in Fig. 5(c), nearly 10–15 % of PIC electrons and 35–50 % of RSM-MP electrons are still within the cluster at this intensity. We now perform PIC and RSM-MP simulations at a higher

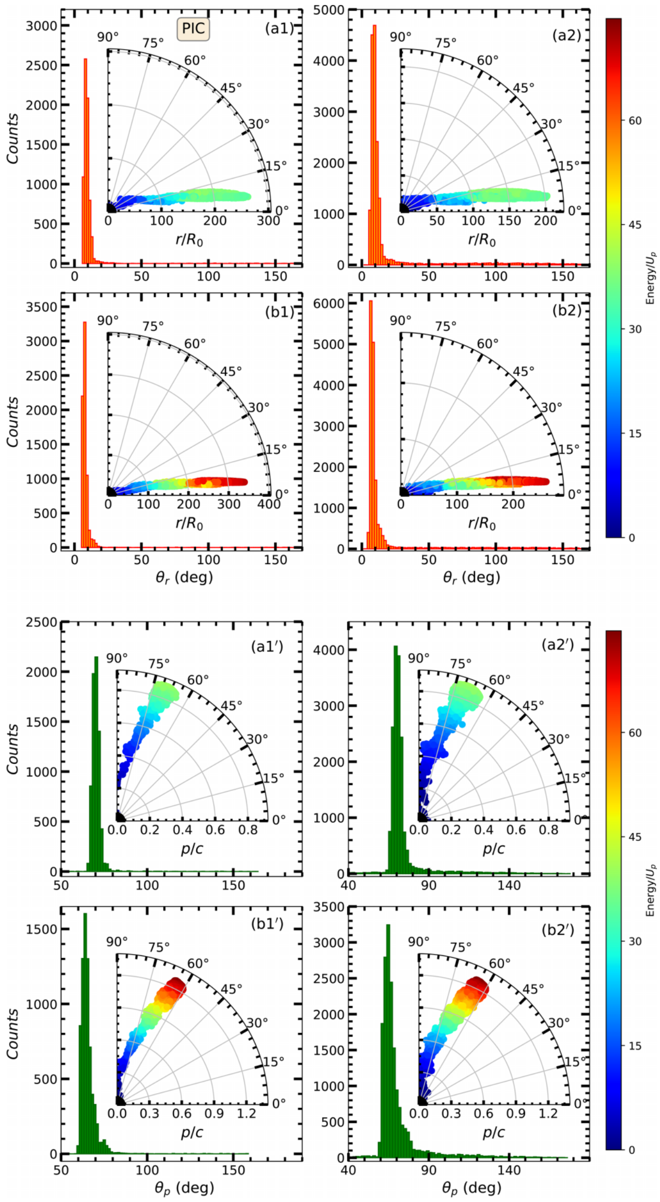

FIG. 6. PIC results for different cluster sizes with $I_0 = 7.13 \times 10^{16}$ W/cm^2. Histograms show the distributions of angular deflections [(a1), (b1), (a2), and (b2)] θ_r in the position space and [(a1′), (b1′), (a2′), and (b2′)] θ_p in the momentum space of PIC electrons. The insets show the respective polar plots with their r/R_0 vs θ_r and p/c vs θ_p corresponding to data points at B and C in Fig. 5(a) with $B_0 = 0.057, 0.07$ a.u. for the $R_0 \approx 3.3$ nm cluster with $N = 7208$ atoms (left column) and the $R_0 \approx 4.4$ nm cluster with $N = 17\,256$ atoms (right column), respectively. Polar coordinates (r, θ_r) and (p, θ_p) of electrons (insets) are color coded with their energy normalized by U_p. Ejected electrons propagate a long distance [(b1) and (b2)] $r = \sqrt{r_\perp^2 + z^2} \approx 350R_0, 280R_0$ with the respective [(b1′) and (b2′)] $p \approx 1.25c, 1.25c$ as conical-spiral beams with narrow angular spreads $\Delta\theta_r < 3^\circ$ and $\Delta\theta_p < 4^\circ$ centered around $\theta_r \approx 7^\circ$–8° and $\theta_p \approx 63^\circ$–$67^\circ$, respectively. The energy of an electron reaches approximately $1.25m_0c^2$ for $\gamma = p/c \approx 1.25$. The other parameters are the same as in Fig. 1.

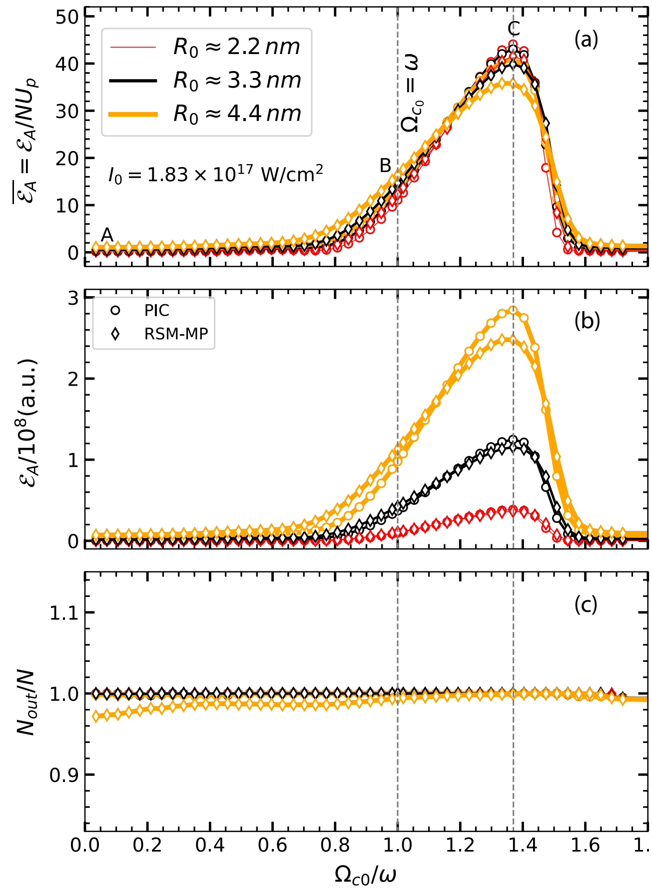

FIG. 7. PIC (○) and RSM (◇) results for different cluster sizes with $I_0 = 1.83 \times 10^{17}$ W/cm^2: (a) average total energy ($\overline{\mathcal{E}_A} = \mathcal{E}_A/NU_\text{p}$) per cluster electron in units of U_p, (b) absorbed total energy $\mathcal{E}_A$ in the cluster scaled down by 10^8, and (c) fractional outer ionization of electrons (N_out/N) vs normalized electron-cyclotron frequency Ω_{c0}/ω for a range of ambient field $|\hat{z}B_\text{ext}| \approx 0$–$2\omega$ for different cluster sizes $R_0 \approx 2.2, 3.3, 4.4$ nm and the respective numbers of atoms $N = 2176, 7208, 17\,256$. Note that $I_0 = 1.83 \times 10^{17}$ W/cm^2 corresponds to greater $U_p = 402.26$ a.u. than in Fig. 5. An absorption peak $44U_\text{p}$ gives an average energy per electron 0.48 MeV. The other parameters are the same as in Fig. 1.

$I_0 = 1.83 \times 10^{17}$ W/cm^2 in the nonrelativistic regime for all three cluster sizes $R_0 = 2.2, 3.3, 4.4$ nm, keeping the other parameters the same as in Fig. 5. The results of absorption per electron $\overline{\mathcal{E}_A} = \mathcal{E}_A/NU_p$ in U_p, total absorption $\mathcal{E}_A$, and outer ionized fraction N_out/N of electrons vs Ω_{c0}/ω are shown in Fig. 7. Compared to Fig. 5, the per electron energies $\overline{\mathcal{E}_A}$ for ejected electrons from different clusters are nearly the same [Fig. 7(a)] and the maximum absorption per electron is now in the range $\overline{\mathcal{E}_A} \approx 44 - 42$ as cluster size increases $R_0 = 2.2$–4.4 nm, but outer ionization reaches 100% for all clusters [Fig. 7(c)] at this higher intensity. The total absorption $\mathcal{E}_A$ in each cluster [Fig. 7(b)] increases more than two times the value in Fig. 5(b). If we compare the ratio of maximum

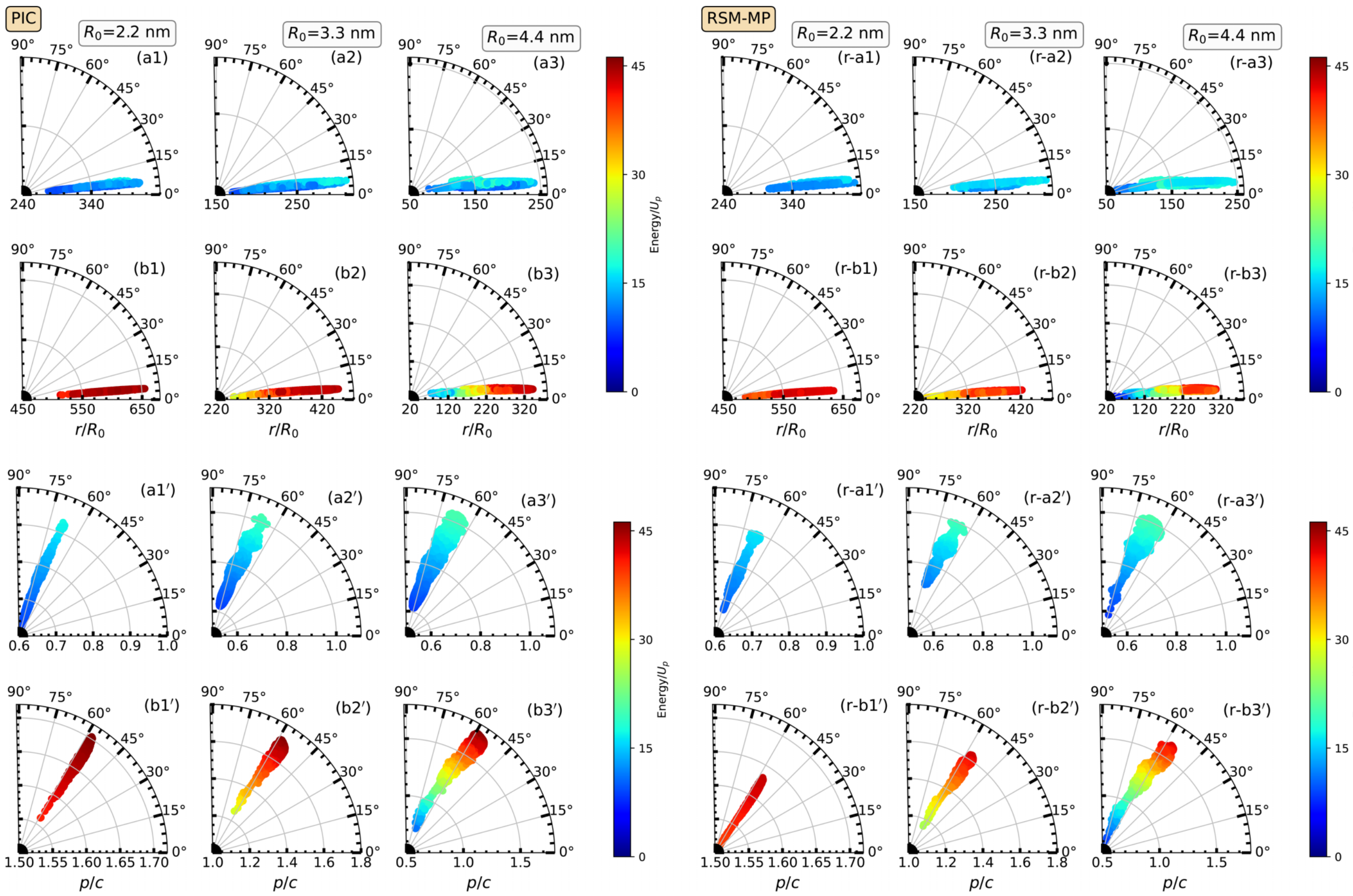

FIG. 8. PIC and RSM results for different cluster sizes (columnwise) with higher $I_0 = 1.83 \times 10^{17}$ W/cm^2. The angular distribution of PIC electrons is shown in the (r, θ_r) and (p, θ_p) planes [(a1)–(a3) and (b1)–(b3) for (r, θ_r); (a1′)–(a3′) and (b1′)–(b3′) for (p, θ_p)] corresponding to those data points at B and C in Fig. 7 for $B_0 = 0.057, 0.078$ a.u., respectively. Polar coordinates (r, θ_r) and (p, θ_p) of electrons are color coded with their energy normalized by U_p. Ejected electrons propagate a long distance beyond $r = \sqrt{r_\perp^2 + z^2} \approx 650R_0, 430R_0, 330R_0$ [(b1)–(b3)] with momentum $p/c > 1.7$ [(b1′)–(b3′)] as conical-spiral beams with narrow angular spreads $\Delta\theta_r < 3^\circ$ and $\Delta\theta_p < 4^\circ$ centered around $\theta_r \approx 6^\circ$–7° and $\theta_p \approx 58^\circ$–$62^\circ$. The RSM-MP electron distributions for all three cluster sizes [(r-a1)–(r-a3) and (r-b1)–(r-b3) for (r, θ_r); (r-a1′)-(r-a3′) and (r-b1′)–(r-b3′) for (p, θ_p)] predict the respective PIC electron distributions accurately. The energy of an electron reaches approximately $1.75m_0c^2$ for $\gamma = p/c \approx 1.75$. The other parameters are the same as in Figs. 1 and 2.

absorption [Fig. 7(b)] for different clusters, we find max $(\mathscr{E}_A) \approx 0.4{:}1.3{:}2.8 \approx 1{:}3.325{:}6.9$, which scales with the number of electrons in the cluster as $N \approx 2176{:}7208{:}17\,256 \approx 1{:}3.3{:}7.9$. Thus N vs max$(\mathscr{E}_A)$ is almost linear at a very high I_0 when outer ionization is 100%. At this high intensity, the RSM-MP results (diamonds) in Fig. 7 also predict the PIC absorption curves very well compared to those in Fig. 5.

In Fig. 8 we compare the distribution of PIC electrons in the (r, θ_r) plane and (p, θ_p) plane (as in Figs. 3 and 6) for three different cluster sizes [for (r, θ_r) in Figs. 8(a1)–8(a3) and 8(b1)–8(b3); and for (p, θ_p) in Figs. 8(a1′)–8(a3′) and 8(b1′)–8(b3′)] corresponding to points B and C in Fig. 7 with $B_0 = 0.057, 0.078$ a.u., respectively. We find that respective electron beams are even narrower within angular ranges of $\Delta\theta_r \approx 3^\circ$–$4^\circ$ and $\Delta\theta_p \approx 58^\circ$–$62^\circ$. Also, with increasing cluster size, electron beams are more intense with a greater number of energetic electrons. At a very high I_0 and ambient B_0 near ECR or RECR, the electron distribution for a bigger cluster becomes very similar to that of a small cluster in the regime of 100% outer ionization. The RSM-MP electron distributions for all three cluster sizes [for (r, θ_r) in Figs. 8(r-a1)–8(r-a3) and 8(r-b1)–8(r-b3); for (p, θ_p) in Figs. 8(r-a1′)–8(r-a3′) and 8(r-b1′)–8(r-b3′)] predict the respective PIC electron distributions accurately.

VI. CONCLUSION

We have studied the interaction of intense 800-nm, 5-fs (FWHM) broadband laser pulses of different intensities $I_0 = (7.13 \times 10^{16})$–$(1.83 \times 10^{17})$ W/cm^2 with deuterium clusters of various sizes (radius $R_0 \approx 2.2$–4.4 nm) in the presence of ambient magnetic fields of strengths $B_0 = 0$–2ω in the laser propagation direction z using 3D hybrid PIC simulations and the RSM. Here laser absorption occurs in two stages, via AHR (first stage) and ECR or relativistic ECR processes (second stage). Auxiliary B_0 enhances the coupling of the laser field to cluster electrons via improved frequency matching for ECR or RECR as well as phase matching [34] for a longer duration covering approximately 50–60 % of the five-cycle laser pulse (in this work) through the pulse maxima. As a result, the average absorbed energy per electron $\overline{\mathscr{E}}$ jumps near $36U_p$–$70U_p$, which is significant. Similar enhancements in energy were also obtained for bigger clusters but were not repeated here for the sake of conciseness. Otherwise, $\overline{\mathscr{E}}$ is mostly limited around $0.5U_p$–$3U_p$ without B_0. Increasing the cluster size (from $R_0 \approx 2.2$ to $R_0 \approx 4.4$ nm) per electron, the energy $\overline{\mathscr{E}}$ remains almost the same (approximately $36U_p$–$70U_p$) near ECR or RECR, but net absorption increases almost linearly with the number of electrons N in the regime of 100% outer ionization at high intensities.

We further analyzed the energy distribution of ejected electrons as well as their angular distribution in position space and momentum space. We found that laser-coupled electrons form a nearly monoenergetic, weakly relativistic conical-spiral beam with a narrow angular spread that traverses a few hundred R_0 (or on the order of λ) with momentum $p/c > 1.7$ in the presence of an ambient magnetic field near ECR or RECR, which may not be possible only with the laser field. Also, as the cluster size increases, the intensity of the electron beam increases with a greater number of energetic electrons at restricted angles of $\theta_r \approx 7^\circ$–10° and $\theta_p \approx 58^\circ$–$62^\circ$ with respect to the z direction for $I_0 = (7.13 \times 10^{16})$–$(1.83 \times 10^{17})$ W/cm^2. Most of the PIC results were justified by RSM simulations.

This work may be important for the fast ignition technique of inertial confinement fusion where an intense collimated relativistic electron beam is required to be transported deep inside the matter with less divergence. Additionally, it may be useful in laser-driven electron accelerators, ultrashort-x-ray sources for radiation therapy, and other medical applications.

ACKNOWLEDGMENTS

Numerical simulations were performed on the Antya Linux cluster of the HPC facility at IPR. The authors acknowledge Dr. Devendra Sharma for a careful reading of the manuscript.

APPENDIX: RIGID-SPHERE MODEL OF A CLUSTER

Details of the rigid-sphere model can be found in earlier works [27–30,33,34,60,71,72]. Here we mention it briefly for better readability of the paper by general readers wherever PIC results are compared with the RSM. In this model, the cluster is considered as a preionized nanoplasma of spherical shape. The radius of the ionic background is assumed to be the same as the initial cluster radius R_0, and the charge density is ρ_i. The corresponding potential $\Phi_I(r)$ and the space-charge field $\boldsymbol{E}_{sc}(\boldsymbol{r})$ are given by

$$\phi_I(r) = \omega_M^2 R_0^2 \begin{cases} 3/2 - r^2/2R_0^2 & \text{for } r \leqslant R_0 \\ R_0/r & \text{for } r > R_0, \end{cases}$$

$$\boldsymbol{E}_{sc}(\boldsymbol{r}) = \begin{cases} \omega_M^2 \boldsymbol{r} & \text{for } r \leqslant R_0 \\ \omega_M^2 R_0^3 \boldsymbol{r}/r^3 & \text{for } r > R_0. \end{cases} \tag{A1}$$

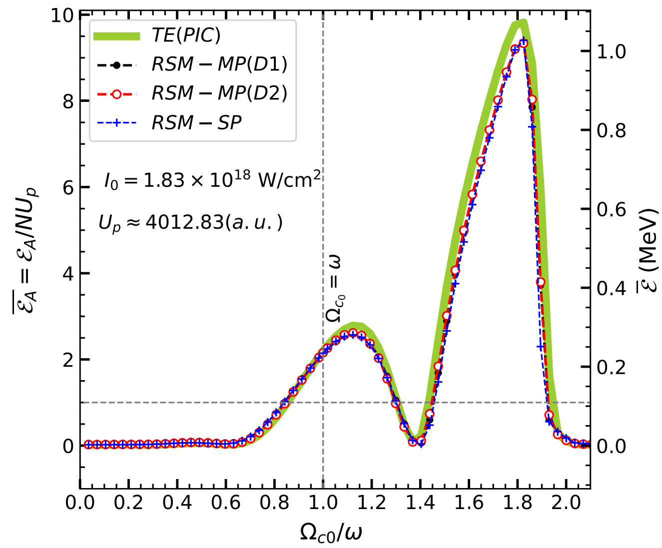

FIG. 9. Comparison of PIC and RSM results at a high intensity. The average total absorbed energy $\overline{\mathscr{E}}_A$ per electron is plotted vs Ω_{c0}/ω for a range of ambient field $|\hat{z}B_{ext}| \approx 0$–$2\omega$ with an $n = 5$ cycle laser pulse of $I_0 \approx 1.83 \times 10^{18}$ W/cm^2 irradiating a deuterium cluster of $N = 2176$ and $R_0 = 2.2$ nm (as in Fig. 1). Energy is shown normalized by the corresponding U_p. At this high $I_0 \approx 1.83 \times 10^{18}$ W/cm^2, the absorption peak is right shifted from the ECR condition $\Omega_{c0} = \omega$ due to relativistic modification of $\Omega_c = \Omega_{c0}/\gamma$ for $\gamma > 1$. Moreover, there is a second peak approximately equal to $10U_p$ giving an average energy per electron of approximately 1.088 MeV (right axis). The RSM results (dashed lines) justify the PIC results very well.

An electron interacts with the ionic field and the applied fields $\boldsymbol{E}_l, \boldsymbol{B}_l, \boldsymbol{B}_{ext}$ obeying the equations of motion

$$\frac{d\boldsymbol{p}}{dt} = q\{[\boldsymbol{E}_l + \boldsymbol{E}_{sc}(\boldsymbol{r})] + \boldsymbol{v} \times (\boldsymbol{B}_l + \boldsymbol{B}_{ext})\}, \tag{A2}$$

$$\frac{d\boldsymbol{r}}{dt} = \boldsymbol{v} = \frac{\boldsymbol{p}}{\gamma m_0}, \tag{A3}$$

$$\frac{d(\gamma m_0 c^2)}{dt} = q\boldsymbol{v} \cdot [\boldsymbol{E}_l + \boldsymbol{E}_{sc}(\boldsymbol{r})], \tag{A4}$$

where $\gamma = 1/\sqrt{1 - v^2/c^2} = \sqrt{1 + p^2/m_0^2c^2}$ is the relativistic γ factor for the electron and $m_0, q, \boldsymbol{r}, \boldsymbol{v}$, and $\boldsymbol{p}$ are its rest mass, charge, position, velocity, and linear momentum, respectively, with $m_0 = 1$ and $q = e = -1$ in a.u. Ions are frozen and their dynamics are neglected in the RSM for the short-pulse duration used in this work. Equations (A2)–(A4) are very similar to those respective equations (2)–(4) of PIC electrons and they are solved with the same field values $(\boldsymbol{E}_l, \boldsymbol{B}_l, \boldsymbol{B}_{ext})$ and cluster parameters (R_0, N) when results are compared.

The RSM with noninteracting electrons

The RSM can be used to study single-electron (call it RSM-SP) dynamics and laser absorption [34]. In the RSM-SP case, assuming initial conditions $\boldsymbol{r} = \boldsymbol{0}$ and $\boldsymbol{v} = \boldsymbol{0}$, an electron remains inside or outside the cluster after the end of the laser pulse. Therefore, the outer-ionization fraction is either 0 or 1, which is not always the case in a realistic multielectron case (e.g., the PIC case). Moreover, all electrons may not have the same final energy, which depends upon the initial distribution of electrons as well. To mimic the multielectron (MP) scenario with the RSM (see also [34] for more discussion) we may distribute all N electrons inside the respective cluster radius R_0 in different ways (randomly, uniformly, and PIC-like), assuming they are mutually noninteracting. We compare these multielectron RSM-MP results with the PIC simulations for the (i) average and total energy absorbed by electrons, (ii) energy distribution of electrons, and (iii) their angular distributions in position and momentum space in the main text. Remarkably, good agreement is obtained in most cases, showing the RSM as a good predictive model, particularly at high laser intensities. For illustration, Fig. 9 shows these comparisons with the RSM-SP, RSM-MP (D1, uniform distribution), and RSM-MP (D2, PIC-like distribution) at higher intensity $I_0 \approx 1.83 \times 10^{18}$ W/cm^2 (similar to Fig. 1 at $I_0 \approx 7.13 \times 10^{16}$ W/cm^2). If not stated explicitly, the RSM-MP uses a PIC-like initial distribution for better comparison with the respective PIC simulation.

[1] T. Ditmire, J. W. G. Tisch, E. Springate, M. B. Mason, N. Hay, J. P. Marangos, and M. H. R. Hutchinson, Phys. Rev. Lett. **78**, 2732 (1997).

[2] T. Ditmire, E. Springate, J. W. G. Tisch, Y. L. Shao, M. B. Mason, N. Hay, J. P. Marangos, and M. H. R. Hutchinson, Phys. Rev. A **57**, 369 (1998).

[3] T. Ditmire, J. W. G. Tish, E. Springate, M. B. Mason, N. Hay, J. Marangos, and M. H. R. Hutchinson, Nature (London) **386**, 54 (1997).

[4] M. Lezius, S. Dobosz, D. Normand, and M. Schmidt, Phys. Rev. Lett. **80**, 261 (1998).

[5] R. Rajeev, T. M. Trivikram, K. P. M. Rishad, V. Narayanan, E. Krishnakumar, and M. Krishnamurthy, Nat. Phys. **9**, 185 (2013).

[6] L. M. Chen, J. J. Park, K. H. Hong, I. W. Choi, J. L. Kim, J. Zhang, and C. H. Nam, Phys. Plasmas **9**, 3595 (2002).

[7] Y. L. Shao, T. Ditmire, J. W. G. Tisch, E. Springate, J. P. Marangos, and M. H. R. Hutchinson, Phys. Rev. Lett. **77**, 3343 (1996).

[8] E. Springate, S. A. Aseyev, S. Zamith, and M. J. J. Vrakking, Phys. Rev. A **68**, 053201 (2003).

[9] L. M. Chen, J. J. Park, K.-H. Hong, J. L. Kim, J. Zhang, and C. H. Nam, Phys. Rev. E **66**, 025402(R) (2002).

[10] A. McPherson, B. D. Thompson, A. B. Borisov, K. Boyer, and C. K. Rhodes, Nature (London) **370**, 631 (1994).

[11] L. M. Chen, F. Liu, W. M. Wang, M. Kando, J. Y. Mao, L. Zhang, J. L. Ma, Y. T. Li, S. V. Bulanov, T. Tajima, Y. Kato, Z. M. Sheng, Z. Y. Wei, and J. Zhang, Phys. Rev. Lett. **104**, 215004 (2010).

[12] J. Jha, D. Mathur, and M. Krishnamurthy, J. Phys. B **38**, L291 (2005).

[13] F. Dorchies, T. Caillaud, F. Blasco, C. Bonté, H. Jouin, S. Micheau, B. Pons, and J. Stevefelt, Phys. Rev. E **71**, 066410 (2005).

[14] V. Kumarappan, M. Krishnamurthy, D. Mathur, and L. C. Tribedi, Phys. Rev. A **63**, 023203 (2001).

[15] C. Rose-Petruck, K. J. Schafer, K. R. Wilson, and C. P. J. Barty, Phys. Rev. A **55**, 1182 (1997).

[16] D. Bauer and A. Macchi, Phys. Rev. A **68**, 033201 (2003).

[17] C. Siedschlag and J. M. Rost, Phys. Rev. A **67**, 013404 (2003).

[18] E. M. Snyder, S. A. Buzza, and A. W. Castleman, Jr., Phys. Rev. Lett. **77**, 3347 (1996).

[19] K. Ishikawa and T. Blenski, Phys. Rev. A **62**, 063204 (2000).

[20] F. Megi, M. Belkacem, M. A. Bouchene, E. Suraud, and G. Zwicknagel, J. Phys. B **36**, 273 (2003).

[21] C. Jungreuthmayer, L. Ramunno, J. Zanghellini, and T. Brabec, J. Phys. B **38**, 3029 (2005).

[22] D. Bauer, J. Phys. B **37**, 3085 (2004).

[23] T. Ditmire, T. Donnelly, A. M. Rubenchik, R. W. Falcone, and M. D. Perry, Phys. Rev. A **53**, 3379 (1996).

[24] I. Last and J. Jortner, Phys. Rev. A **60**, 2215 (1999).

[25] U. Saalmann and J.-M. Rost, Phys. Rev. Lett. **91**, 223401 (2003).

[26] T. Fennel, G. F. Bertsch, and K.-H. Meiwes-Broer, Eur. Phys. J. D **29**, 367 (2004).

[27] P. Mulser and M. Kanapathipillai, Phys. Rev. A **71**, 063201 (2005).

[28] P. Mulser, M. Kanapathipillai, and D. H. H. Hoffmann, Phys. Rev. Lett. **95**, 103401 (2005).

[29] M. Kundu and D. Bauer, Phys. Rev. A **74**, 063202 (2006).

[30] M. Kundu and D. Bauer, Phys. Rev. Lett. **96**, 123401 (2006).

[31] I. Kostyukov and J.-M. Rax, Phys. Rev. E **67**, 066405 (2003).

[32] T. Taguchi, T. M. Antonsen, and H. M. Milchberg, Phys. Rev. Lett. **92**, 205003 (2004).

[33] S. S. Mahalik and M. Kundu, Phys. Plasmas **23**, 123302 (2016).

[34] K. Swain, S. S. Mahalik, and M. Kundu, Sci. Rep. **12**, 11256 (2022).

[35] P. B. Corkum, Phys. Rev. Lett. **71**, 1994 (1993).

[36] P. Moreno, L. Plaja, and L. Roso, Europhys. Lett. **28**, 629 (1994).

[37] P. Moreno, L. Plaja, and L. Roso, Phys. Rev. A **55**, R1593 (1997).

[38] M. Lein and J. M. Rost, Phys. Rev. Lett. **91**, 243901 (2003).

[39] M. Shaikh, A. D. Lad, K. Jana, D. Sarkar, I. Dey, and G. R. Kumar, Plasma Phys. Contr. Fusion **59**, 014007 (2017).

[40] V. V. Ivanov, A. V. Maximov, R. Betti, L. S. Leal, J. D. Moody, K. J. Swanson, and N. A. Huerta, Matter Radiat. Extremes **6**, 046901 (2021).

[41] S. Fujioka, Z. Zhang, K. Ishihara, K. Shigemori, Y. Hironaka, T. Johzaki, A. Sunahara, N. Yamamoto, H. Nakashima, T. Watanabe, H. Shiraga, H. Nishimura, and H. Azechi, Sci. Rep. **3**, 1170 (2013).

[42] D. Nakamura, A. Ikeda, H. Sawabe, Y. H. Matsuda, and S. Takeyama, Rev. Sci. Instrum. **89**, 095106 (2018).

[43] M. Murakami, J. J. Honrubia, K. Weichman, A. V. Arefiev, and S. V. Bulanov, Sci. Rep. **10**, 16653 (2020).

[44] T. C. Wilson, Z.-M. Sheng, B. Eliasson, and P. McKenna, Plasma Phys. Contr. Fusion **63**, 084001 (2021).

[45] A. Longman and R. Fedosejevs, Phys. Rev. Res. **3**, 043180 (2021).

[46] Y. Shi, H. Qin, and N. J. Fisch, Phys. Plasmas **25**, 055706 (2018).

[47] Z. Gong, F. Mackenroth, T. Wang, X. Q. Yan, T. Toncian, and A. V. Arefiev, Phys. Rev. E **102**, 013206 (2020).

[48] K. Weichman, A. P. L. Robinson, M. Murakami, and A. V. Arefiev, New J. Phys. **22**, 113009 (2020).

[49] M. Tatarakis, I. Watts, F. N. Beg, E. L. Clark, A. E. Dangor, A. Gopal, M. G. Haines, P. A. Norreys, U. Wagner, M.-S. Wei, M. Zepf, and K. Krushelnick, Nature (London) **415**, 280 (2002).

[50] M. Tatarakis, A. Gopal, I. Watts, F. N. Beg, A. E. Dangor, K. Krushelnick, U. Wagner, P. A. Norreys, E. L. Clark, M. Zepf, and R. G. Evans, Phys. Plasmas **9**, 2244 (2002).

[51] S. L. Shapiro and S. A. Teukolsky, *Black Holes, White Dwarfs, and Neutron Stars: The Physics of Compact Objects* (Wiley-VCH, Weinheim, 1983).

[52] S. Mondal, V. Narayanan, W. J. Ding, A. D. Lad, B. Hao, S. Ahmad, W. M. Wang, Z. M. Sheng, S. Sengupta, P. Kaw, A. Das, and G. R. Kumar, Proc. Natl. Acad. Sci. USA **109**, 8011 (2012).

[53] O. V. Gotchev, J. P. Knauer, P. Y. Chang, N. W. Jang, M. J. Shoup III, D. D. Meyerhofer, and R. Betti, Rev. Sci. Instrum. **80**, 043504 (2009).

[54] P. Y. Chang, G. Fiksel, M. Hohenberger, J. P. Knauer, R. Betti, F. J. Marshall, D. D. Meyerhofer, F. H. Séguin, and R. D. Petrasso, Phys. Rev. Lett. **107**, 035006 (2011).

[55] M. Hohenberger, P.-Y. Chang, G. Fiksel, J. P. Knauer, R. Betti, F. J. Marshall, D. D. Meyerhofer, F. H. Séguin, and R. D. Petrasso, Phys. Plasmas **19**, 056306 (2012).

[56] T. Iwawaki, H. Habara, S. Baton, K. Morita, J. Fuchs, S. Chen, M. Nakatsutsumi, C. Rousseaux, F. Filippi, W. Nazarov, and K. A. Tanaka, Phys. Plasmas **21**, 113103 (2014).

[57] S. Malko, X. Vaisseau, F. Perez, D. Batani, A. Curcio, M. Ehret, J. Honrubia, K. Jakubowska, A. Morace, J. J. Santos, and L. Volpe, Sci. Rep. **9**, 14061 (2019).

[58] Y. Malkov, A. Stepanov, D. Yashunin, L. Pugachev, P. Levashov, N. Andreev, K. Platonov, and A. Andreev, High Power Laser Sci. Eng. **1**, 80 (2013).

[59] M. Kundu, P. K. Kaw, and D. Bauer, Phys. Rev. A **85**, 023202 (2012).

[60] S. S. Mahalik and M. Kundu, Phys. Rev. A **97**, 063406 (2018).

[61] M. Kundu, S. V. Popruzhenko, and D. Bauer, Phys. Rev. A **76**, 033201 (2007).

[62] S. V. Popruzhenko, M. Kundu, D. F. Zaretsky, and D. Bauer, Phys. Rev. A **77**, 063201 (2008).

[63] M. Kundu and D. Bauer, Phys. Plasmas **15**, 033303 (2008).

[64] M. Kundu, Ph.D. thesis, Ruprecht-Karls-Universität, 2007.

[65] H. Bethe and E. Salpeter, *Quantum Mechanics of One and Two Electron Atoms* (Springer, Berlin, 1957).

[66] A. V. Arefiev, A. P. L. Robinson, and V. N. Khudik, J. Plasma Phys. **81**, 475810404 (2015).

[67] A. Pukhov, Z.-M. Sheng, and J. Meyer-ter Vehn, Phys. Plasmas **6**, 2847 (1999).

[68] G. D. Tsakiris, C. Gahn, and V. K. Tripathi, Phys. Plasmas **7**, 3017 (2000).

[69] H. S. Ghotra and N. Kant, Phys. Plasmas **23**, 013101 (2016).

[70] H. S. Ghotra and N. Kant, Laser Phys. Lett. **15**, 066001 (2018).

[71] S. R. Krishnan, L. Fechner, M. Kremer, V. Sharma, B. Fischer, N. Camus, J. Jha, M. Krishnamurthy, T. Pfeifer, R. Moshammer, J. Ullrich, F. Stienkemeier, M. Mudrich, A. Mikaberidze, U. Saalmann, and J.-M. Rost, Phys. Rev. Lett. **107**, 173402 (2011).

[72] S. R. Krishnan, R. Gopal, R. Rajeev, J. Jha, V. Sharma, M. Mudrich, R. Moshammer, and M. Krishnamurthy, Phys. Chem. Chem. Phys. **16**, 8721 (2014).